

# Critical Role of High-lying Triplet States for Efficient Excitons Utilization in High-Performance Non-doped Deep-blue Fluorescent and Hybrid White Organic Light-Emitting Diodes

*Baoxi Li, Ganggang Li, Han Zhang, Haozhong Wu, Kongqi Chen, Zhiming Wang\*, and Ben Zhong Tang\**

B. Li and G. Li contributed equally to this work

B. Li, G. Li, H. Zhang, H. Wu, K. Chen, Prof. Z. Wang, Prof. B. Z. Tang  
AIE Institute, State Key Laboratory of Luminescent Materials and Devices,  
Guangdong Provincial Key Laboratory of Luminescence from Molecular Aggregates,  
Center for Aggregation-Induced Emission,  
South China University of Technology (SCUT),  
Guangzhou 510640, China  
E-mail: wangzhiming@scut.edu.cn; tangbenz@cuhk.edu.cn

Prof. B. Z. Tang  
Shenzhen Institute of Aggregate Science and Technology,  
School of Science and Engineering,  
The Chinese University of Hong Kong, Shenzhen,  
Shenzhen 518172, China  
E-mail: tangbenz@cuhk.edu.cn

**Keywords:** (hot exciton, high-lying triplet state, deep-blue OLEDs, two-color hybrid WOLEDs)

**Abstract:** For organic light-emitting diodes (OLEDs), the characteristics of high-lying excited states of pure organic materials significantly affect the utilization of triplet excitons, which are critical in the process of electroluminescence. Herein, two novel molecules, PT-1 and PT-2, with deep-blue emission were obtained, which exhibited nearly identical photophysical behavior in the photoluminescence process. However, the remarkable distinction in the characteristics of the high-lying triplet excited states between PT-1 and PT-2 led to a significant difference in the electroluminescence performance. Moreover, the non-doped OLED based on PT-1 exhibited maximum external quantum efficiency ( $\eta_{\text{ext}}$ ) of 6.63% with a

low efficiency roll-off. In addition, we employed PT-1 as the phosphorescent host materials to fabricate two-color hybrid white OLEDs (WOLEDs), from which we can realize the transformation from warm-white to quasi-white light by tuning the thickness of emission layer, with maximum  $\eta_{\text{ext}}$  and power efficiency ( $\eta_p$ ) of 23.93% / 84.37 lm W<sup>-1</sup> and 10.49% / 33.96 lm W<sup>-1</sup>, respectively. These results deepen demonstrate the effects of high-lying excited states on electroluminescence and facilitate the preparation of functional OLEDs.

## 1. Introduction

Since the invention of organic light-emitting diodes (OLEDs),<sup>[1]</sup> this display technology has been vigorously researched, and large-scale commercial applications have also been achieved. Thus far, high-performance deep-blue OLEDs are particularly important for improving the color gamut and white lighting.<sup>[2]</sup> According to the limit of spin statistics, only 25% of electron-hole pairs are converted into singlet excitons, and the remaining 75% triplet excitons cannot be harnessed in pure organic conventional fluorescent materials, which lead to the upper limit of OLED efficiency. The subsequent development of phosphorescent, triplet-triplet annihilation (TTA), thermally activated delayed fluorescent (TADF), and “hot exciton” materials effectively utilize triplet excitons through special molecular designs. However, owing to the existence of relatively weaker coordination bonds and a slow exciton decay process for phosphorescent materials, the stability of the devices is significantly affected in the deep-blue region.<sup>[3]</sup> To realize the utilization of triplet excitons, there are some specific requirements on the energy level of the excited state for the other three types of pure organic materials. Considering the energy level,  $T_2 > 2T_1 \geq S_1$  should be realized in the excited state level as much as possible for TTA materials, which will significantly improve

the channel for producing singlet excitons in TTA.<sup>[4]</sup> TADF materials can realize efficient up-conversion from triplet excitons to singlet excitons by constructing a very small energy gap between the  $S_1$  and  $T_1$  states,<sup>[5]</sup> and the reverse intersystem crossing (RISC) process can be promoted by non-adiabatic coupling between a charge-transfer triplet ( $^3CT$ ) state and a local triplet ( $^3LE$ ) state.<sup>[6]</sup> Furthermore, as for “Hot exciton” materials, it harnesses the triplet excitons through hRISC channels from triplet excitons at high-lying states ( $T_n \geq 2$ ) to singlet excitons ( $S_m \geq 1$ ). To facilitate the activation of hRISC channels, it is necessary to suppress the internal conversion (IC) process of  $T_n \rightarrow T_1$  and accelerate the rates of hRISC.<sup>[7]</sup> Therefore, although the excited states of high energy levels usually have little effect on the fluorescence in the photoluminescence process according to Kasha’s rule, the characteristics of high-lying excited states are crucial in the performance of electroluminescence.<sup>[8]</sup>

Herein, we report two novel deep-blue molecules, PT-1 and PT-2. The molecules exhibited nearly identical photophysical behavior in the photoluminescence process. However, owing to the remarkable distinction in the characteristics of the high-lying triplet excited states between PT-1 and PT-2, PT-1 can capture triplet excitons more effectively, exhibiting outstanding electroluminescence performance. Furthermore, because PT-1 with deep-blue emission shows high performance in non-doped devices, we further employed PT-1 as the host of phosphorescent materials for PhOLEDs and two-color hybrid WOLEDs. The yellow and red phosphorescent OLEDs possess maximum external quantum efficiency ( $\eta_{ext}$ ) of 23.28% and 13.27%, respectively, accompanied by low efficiency roll-off. Along with the change of the thicknesses of the phosphorescent-layers, the two-color hybrid white light devices can realize the transformation from warm-white to quasi-white light, and the corresponding maximum

$\eta_{\text{ext}} / \eta_{\text{p}}$  are 23.93% / 84.37 lm W<sup>-1</sup> and 10.49% / 33.96 lm W<sup>-1</sup>. These results intuitively prove that the construction of high-lying triplet states has an important influence on the performance of electroluminescence, and outstanding performance was successfully achieved in the deep-blue OLEDs and two-color hybrid WOLEDs.

## 2. Results and Discussion

### 2.1. Synthesis and Characterizations

The synthetic routes of PT-1 and PT-2 are shown in **Scheme S1** in the Supporting Information. According to the previously reported literature,<sup>[7b]</sup> the brominated compound, PPIBr, of PPI with excellent properties of the deep-blue group was obtained via a one-pot reaction. PPIB was obtained by the reaction of PPIBr and bis(pinacolato)diboron reagents under the catalysis of Pd(dppf)Cl<sub>2</sub> as the catalyst. Finally, PT-1 and PT-2 were synthesized via the Suzuki coupling reaction of TAZ-1/2 and PPIB in high yields. These molecular structures were characterized and verified by NMR and high-resolution mass spectrometry. The detailed synthetic procedures and characterization data are provided in the Supporting Information.

### 2.2. Thermal and Electrochemical Properties

Thermal properties were examined via thermogravimetric analysis (TGA) and differential scanning calorimetry (DSC). As shown in **Figure S1**, PT-1 and PT-2 exhibited good thermodynamic stability, and the corresponding decomposition temperatures ( $T_{\text{d}}$ , corresponding to 5% weight loss) of PT-1 and PT-2 were 496 and 515 °C, respectively. Furthermore, high glass transition temperatures ( $T_{\text{g}}$ ) of 153 and 149 °C were also observed.

The results indicate that they are more conducive to the formation of a uniform evaporation film during the fabrication of OLEDs, which ensures the stability of the device performance.

The electrochemical properties of PT-1 and PT-2 were investigated via cyclic voltammetry (CV) measurements. As shown in Figure S2, according to their oxidation and reduction onsets against Fc/Fc<sup>+</sup> redox couple, based on the equation of Ionization Potential ( $IP_{CV} = [E_{ox} - E_{1/2}(Fc/Fc^+) + 4.8]$  eV, Electron Affinities ( $EA_{CV} = [E_{red} - E_{1/2}(Fc/Fc^+) + 4.8]$  eV, the corresponding the values of  $IP_{CV}$  for PT-1 and PT-2 are calculated to be 5.52 and 5.52 eV, respectively, whereas the values of  $EA_{CV}$  are 2.38 and 2.39 eV. Their thermal and electrochemical properties are summarized in Table 1.

### 2.3. Theoretical Calculation

To analyze the configuration and frontier molecular orbital distributions of the molecules, the ground-state ( $S_0$ ) geometries of PT-1 and PT-2 in the gas phase were optimized at the level of B3LYP/6-31G (d, p) via density functional theory (DFT) calculations using the Gaussian 16 software. As shown in Figure 1b, the optimized ground-state ( $S_0$ ) geometry exhibits that the torsion angle between the benzene ring extending from the C site of the imidazole ring and imidazole is 27.29° or 26.75°, which corresponds to the  $\theta_2$  of the PT-1 and PT-2 molecules, respectively. This is because imidazole is a five-membered ring with a small steric hindrance. It is beneficial to obtain molecules with good planarity and achieve high fluorescence efficiency by modifying other groups in this direction. PT-1 and PT-2 are composed of C3- and N1- substitution directions of 1, 2, 4-triazole in this extension direction, respectively. Compared with that of PT-1,  $\theta_3$  of PT-2 exhibits a larger torsion angle (45.72°) because the benzene ring connected to the triazole N1- substitute of PT-2 is affected by the surrounding

benzene ring. Furthermore, these molecules exhibit hybrid molecular frontier orbitals, as shown in **Figure 1c**, and the highest occupied molecular orbitals (HOMOs) are mainly distributed on Phenanthroimidazole, while the lowest unoccupied molecular orbitals (LUMOs) are mainly located in triazole units and overlaps with each other significantly on the intermediate benzene rings. In addition, the excited state properties of these molecules were further explored based on  $S_1$  geometries via time-dependent DFT (TDDFT) using M06-2X/def-TZVP. As shown in **Figure S3**, the natural transition orbitals (NTOs) of the excited states show that the particles and holes of the  $S_1$  state for the two molecules exhibit the same distribution as the hybridized local and charge-transfer (HLCT) nature, and the  $T_1$  state shows an electron configuration similar to that of the  $S_1$  state. However, the energy levels of the two molecules present different distributions in the high-lying triplet states, which may result in differences in the electroluminescence performance.

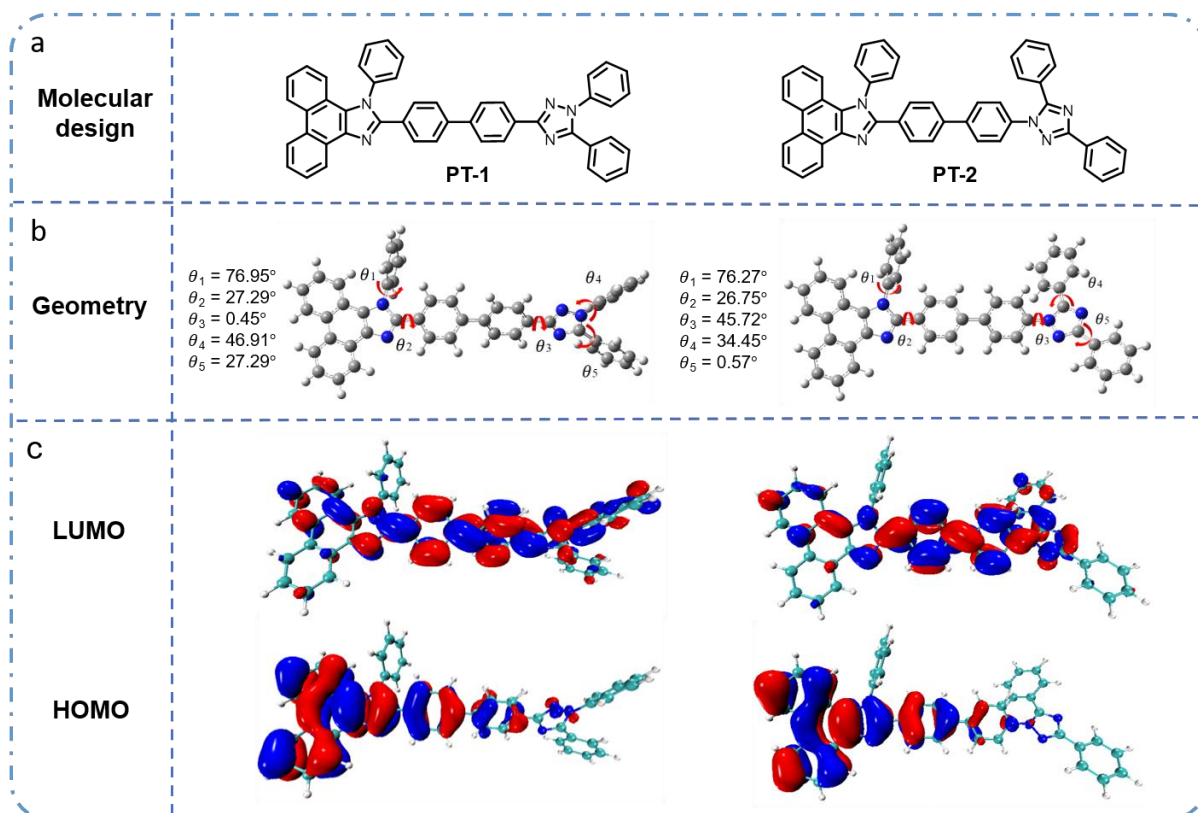


**Figure 1.** (a) Molecular design, (b) optimized  $S_0$  geometries, (c) frontier orbital distributions of PT-1 and PT-2.

## 2.4. Photophysical Properties

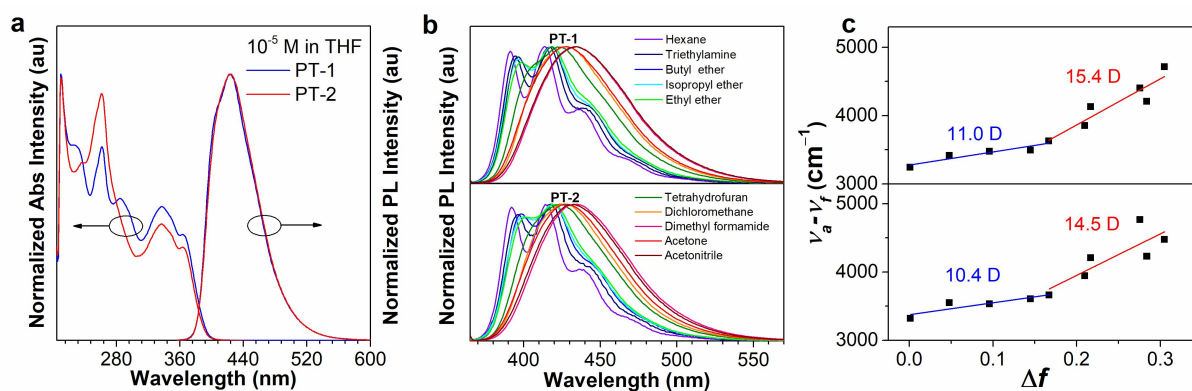


**Figure 2.** (a) Absorption spectra and PL spectra of PT-1 and PT-2 in THF solutions (10<sup>-5</sup> M). (b) The solvatochromic PL spectra of PT-1 and PT-2. (c) Solvatochromic Lippert–Mataga models of PT-1(up) and PT-2(down).

**Table 1.** Optical, thermal, and electronic properties of PT-1 and PT-2.

$\lambda_{\text{abs}}$ [nm]	$\lambda_{\text{em}}$ [nm]		$\eta_{\text{PL}}^{[c]}$ [%]		$E_{\text{S1}}/E_{\text{T1}}$	$T_g/T_d$ [°C]	EAcv/IPcv <sup>[d]</sup> [eV]
	soln <sup>[a]</sup>	film <sup>[b]</sup>	soln <sup>[a]</sup>	film <sup>[b]</sup>			

PT-1	364	423	441	86.3	62.5	3.09/2.31	153/496	2.38/5.52
PT-2	364	423	449	86.5	72.3	3.09/2.36	149/515	2.39/5.52

<sup>a)</sup>In THF solution ( $10^{-5}$  M). <sup>b)</sup>Film = vacuum-deposited neat film. <sup>c)</sup>Fluorescence quantum yield, determined by a calibrated integrating sphere. <sup>d)</sup>Determined by CV measurement in solutions.

**Figure 2a** shows the absorption spectra of PT-1 and PT-2 in dilute THF solutions ( $10^{-5}$  M). The absorption peaks with fine structures at 364 and 260 nm are attributed to the  $\pi$ - $\pi^*$  transition of the phenanthroimidazole (PI) group.<sup>[9]</sup> Compared with the absorption spectrum of 1,3,5-triphenyl-1H-1,2,4-triazole (TPT), as shown in **Figure S5**, the corresponding absorption bands of 211 and 243 nm with the  $\pi$ - $\pi^*$  transition character of the two molecules can be found. However, the absorption band of the ICT state is not clear, which can be attributed to the weak electron-donating and accepting abilities of the PI and triazole groups. To investigate the properties of the excited state  $S_1$  further, the PL spectra of PT-1 and PT-2 were obtained in solvents with various polarities (**Figure 2b**). The maximum emission peaks and peak shapes of the two molecules exhibited similar variations in different polar solvents. Moreover, from n-hexane to acetonitrile, the red-shifts of PT-1 and PT-2 were 20 and 18 nm, respectively. Meanwhile, it can be inferred from the PL spectra that they both show the emission of the LE state with a fine structure at low polarity. With the increase in solvent polarity, the emission spectrum red-shifts and shows the unimodal peak emission of the CT state.

To estimate the dipole moments of the excited state of PT-1 and PT-2 further,<sup>[10]</sup> the change in the Stokes shift ( $\nu_a - \nu_f$ ) with the solvent polarity ( $f$ ) in different solvents is drawn based on the Lippert-Mataga solvatochromic model (**Figure 2c**). They can fit two



straight lines with different slopes in low-polarity solvents ( $f \leq 0.167$ ) and high polarity solvents ( $f \geq 0.21$ ). For PT-2, the dipole moment of the excited state is 10.4 D in low polarity solvents and 14.6 D in high-polarity solvents. The value exhibits the dominant LE component in low-polarity solvents and the dominant CT component in high-polarity solvents. Compared with PT-2, the value of dipole moments ( $\mu_e$ ) of PT-1 fitted by the model is 11.0 D in low-polarity solvents and 15.4 D in high-polarity solvents, indicating that both have similar HLCT characteristics in the excited state. In comparison with the typical CT molecule DMABN with  $\mu_e = 23$  D,<sup>[11]</sup> the  $\mu_e$  values of the two molecules are much smaller. Therefore, the maximum emission peaks and peak shapes of them are basically identical in the THF solution, which can be attributed to the  $S_1$  state of the two molecules in THF solution would exhibit a similar transition mode from PI to triazole units and overlapped to each other to a large extent on the intermediate benzene rings.

The absolute photoluminescence (PL) efficiency ( $\eta_{PL}$ ) values of PT-1 and PT-2 in dilute THF solutions ( $10^{-5}$  M) were tested to be 86.3% and 86.5%, respectively. Moreover, in neat films, these molecules show deep-blue fluorescence emission peaks at 441 and 449 nm and simultaneously possess high-quality  $\eta_{PL}$  of 62.5% and 72.3%, corresponding to PT-1 and PT-2. As shown in Table 1, the energy levels of  $S_1$  and  $T_1$  state were obtained by testing their fluorescence and phosphorescence emission peak in toluene at low temperature (Figure S6, Supporting Information), and their  $\Delta E_{ST}$  were calculated to be 0.78 and 0.73 eV, respectively. The large energy gap between the  $S_1$  and  $T_1$  states of these molecules ruled out the possibility of TADF materials. Furthermore, the transient PL decay spectra also supported the emission of the fluorescence process (Figure S7, Supporting Information).

## 2.5. Non-Doped and Doped Deep-Blue Fluorescence OLEDs

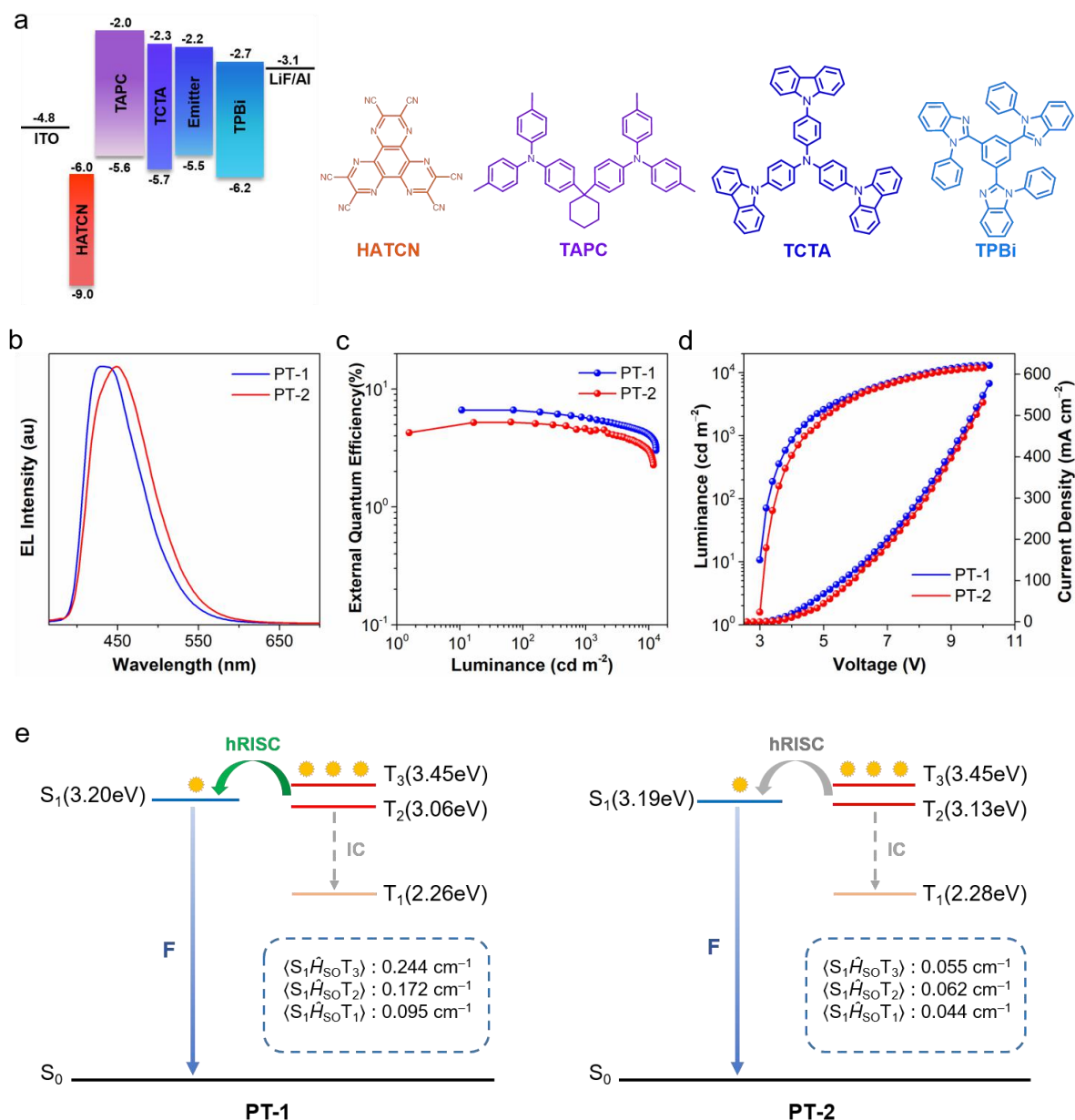


**Figure 3.** (a) Device structure and energy level diagrams for each layer of material. (b) EL spectra, (c) external quantum efficiency versus luminance curves and (d) current density–voltage–luminance (J–V–L) characteristics of the OLEDs based on PT-1 and PT-2. e) Proposed “hot exciton” mechanism based on the PT-1 and PT-2 emitters. S: singlet state; T: triplet state; F: fluorescence; IC: internal conversion; hRISC: reverse intersystem crossing from high-lying triplet state.  $\langle S_m \hat{H}_{SO} T_n \rangle$ : the spin orbit coupling (SOC) values of  $S_m$  state and  $T_n$  state.

**Table 2.** EL performances of deep-blue OLEDs based on PT-1 and PT-2.

EML	Device	$\lambda_{\text{EL}}^{[a]}$ [nm]	$V_{\text{on}}^{[b]}$ [V]	$L^{[c]}$ [cd m <sup>-2</sup> ]	$\eta_c^{[c]}$ [cd A <sup>-1</sup> ]	$\eta_p^{[c]}$ [lm W <sup>-1</sup> ]	$\eta_{\text{ext}}^{[c]}$ [%]	CIE (x, y) <sup>[d]</sup>
ITO/HATCN (5 nm)/TAPC (50 nm)/TCTA (5 nm)/EML (20 nm)/TPBi (40 nm)/LiF (1 nm)/Al (120 nm)								
PT-1	N1	432	3.0	13032	4.94	5.18	6.63/5.78	(0.149, 0.114)
PT-2	N2	446	3.0	5030	5.14	5.01	5.24/4.62	(0.150, 0.147)
CBP: 20% PT-1	D1	414	3.2	3567	3.02	2.97	6.72/5.61	(0.151, 0.072)
CBP: 20% PT-2	D2	414	3.2	4731	2.86	2.69	5.32/4.56	(0.151, 0.082)

<sup>[a]</sup> $\lambda_{\text{EL}}$  = EL maximum. <sup>[b]</sup> $V_{\text{on}}$  = turn-on voltage at 1 cd m<sup>-2</sup>. <sup>[c]</sup>The luminescence ( $L$ ), current efficiency ( $\eta_c$ ), power efficiency ( $\eta_p$ ), external quantum efficiency ( $\eta_{\text{ext}}$ ), <sup>[d]</sup>CIE = Commission Internationale de L'Eclairage, recorded at 10 mA cm<sup>-2</sup>.

As shown in **Figure 3a**, the two molecules **were** used as emitting layers (**EMLs**) to fabricate non-doped deep-blue OLEDs (devices N1 and N2) with an indium tin oxide (ITO)/HATCN (5 nm)/ TAPC (50 nm)/TCTA (5 nm)/EML (20 nm)/TPBi (40 nm)/LiF (1 nm)/Al (120 nm) configuration, where 1,4,5,8,9,11-hexaazatriphenylenehexacarbonitrile (HATCN), di-(4-(N,N-ditolyl-amino)-phenyl) cyclohexane (TAPC), tris(4-carbazoyl-9-ylphenyl)amine (TCTA), 1,3,5-tris-(N-phenylbenzimidazol-2-yl)benzene (TPBi), and LiF functioned as the hole injection, hole-transporting, exciton-blocking, electron-transporting, and electron-injection layers, respectively. The relevant data of electroluminescent device performance are listed in **Table 2**; the turn-on voltage of these devices is 3.0 V, such a low turn-on voltage indicates reasonable energy level matching between the EML layer and functional layer, **as well as** efficient exciton recombination in the EML layer. PT-1 and PT-2 **radiate** deep-blue light with EL **peaks at** 432 and 446 nm, respectively. The maximum  $\eta_{\text{ext}}$  values of the non-doped OLEDs based on PT-1 and PT-2 **were** 6.63% and 5.24%, respectively. Moreover, the N1 and N2 **devices** simultaneously possess very low efficiency

roll-off at a luminance level of 1000 cd m<sup>-2</sup>. According to equation 1, the efficiency of radiative exciton production ( $\eta_r$ ) can be estimated as follows:<sup>[12]</sup>

$$\eta_{\text{ext}} = \gamma \times \eta_{\text{PL}} \times \eta_r \times \eta_{\text{out}}$$

where  $\gamma$  is the electron-hole charge balance factor (ideally, this value is taken to be 100%, provided that the electrons and holes are completely recombined to form excitons in the EML layer) and  $\eta_{\text{out}}$  is the light extraction efficiency ( $\approx 20\%$ ). Because PT-1 and PT-2 show high-quality  $\eta_{\text{PL}}$  of 62.5% and 72.3% in vacuum-deposited neat films, respectively, it can be concluded that the PT-1 emitter can achieve maximum exciton utilization ( $\eta_r = 53.0\%$ ) in the non-doped device, whereas that of PT-2 was 36.2%. The performance of doped devices based on these molecules is summarized in Table S4, and the doped devices were optimized by changing the host material and tuning the doping concentration. The best result was obtained for the ITO/HATCN (5 nm)/TAPC (50 nm)/TCTA (5 nm)/CBP: 20% PT-1/PT-2 (20 nm)/TPBi (40 nm)/LiF (1 nm)/Al (120 nm), where CBP(4,4'-bis(9H-carbazol-9-yl) biphenyl) is the host material. In the doped devices, both show an EL emission peak at 414 nm, with CIE coordinates of (0.151, 0.072) for PT-1 and (0.151, 0.082) for PT-2. Compared with the non-doped devices, the emission peaks of the doped devices show blue-shifted, and the y coordinate of CIE decreases to less than 0.1, which is close to the National Television Standards Committee (NTSC) blue color standard. The radiative exciton-utilizing efficiency of 38.9% and 29.3% for devices D1 and D2, respectively. The decrease in exciton utilization of doped devices may be because the energy of  $T_{2, \text{guest}} > T_{1, \text{host}} (2.56 \text{ eV}) > T_{1, \text{guest}}$ , resulting in the loss of triplet excitons through efficient high-level Dexter energy transfer channels.<sup>[13]</sup>

The exciton utilization of these devices exceeded the spin limit of 25% from the results of the above devices, which indicates that the triplet exciton is effectively utilized. As shown in **Figure 3e**, because PT-1 and PT-2 possess a large energy gap between  $S_1$  and  $T_1$ , and the short single-exponential fluorescence decay lifetimes in the time-resolved PL decay spectrum, the possibility of the TADF mechanism is excluded. Moreover, because the energy level of the  $T_2$  state is more border on the  $S_1$  state for these molecules, and the large energy gap between  $T_2$  and  $T_1$  of the two molecules, 0.80 and 0.85 eV respectively, the hRISC process from high-energy triplet state to singlet state can capture triplet excitons more effectively,<sup>[14]</sup> which explains the efficient exciton utilization via the “hot exciton” mechanism.<sup>[15]</sup>

Furthermore, these molecules exhibit similar photophysical behavior in the photoluminescence process, and even PT-2 has better  $\eta_{PL}$  than PT-1 in a neat film. However, PT-1 possesses higher exciton utilization. It can be observed from the theoretical calculation that although the energy level distribution and the natural transition orbital distribution of the  $S_1$  state are fully similar for the two molecules, the electron and hole distribution as well as transition direction of  $T_2$  and  $T_3$  present significant differences. This can be attributed to PT-1 and PT-2 connected with PI in the substituted direction of C3 and N1 of triazole, respectively. Moreover, the transition direction of TPT is attributed to the substitution of C3 with the triazole ring (**Figure S4**, Supporting Information). Subject to the transition direction of triazole, the natural transition orbitals of the  $T_2$  /  $T_3$  states for PT-1 and PT-2 were significantly different on triazole. The transition direction of the  $T_2$  state for PT-1 originates from the superposition of the entire molecular skeleton and triazole transition, whereas the transition direction of PT-2 tends to transition from triazole to biphenyl between the PI and

triazole. The spin-orbit coupling (SOC) values between the  $T_2/T_3$  and  $S_1$  states of PT-1 and PT-2 are listed in **Figure 3e** and **Table S1** of the Supporting Information. Additionally, the SOC values differ for the two molecules because of the significant difference in the distribution of electrons and holes between the  $T_2$  and  $T_3$  states.

The calculated values of SOC between the  $T_2/T_3$  and the  $S_1$  states for PT-1 are  $0.172\text{ cm}^{-1}$  ( $\langle S_1 \hat{H}_{SO} T_2 \rangle$ ) and  $0.244\text{ cm}^{-1}$  ( $\langle S_1 \hat{H}_{SO} T_3 \rangle$ ), respectively. Compared with PT-1, the SOC of PT-2 is much smaller, with values of  $0.062\text{ cm}^{-1}$  ( $\langle S_1 \hat{H}_{SO} T_2 \rangle$ ) and  $0.055\text{ cm}^{-1}$  ( $\langle S_1 \hat{H}_{SO} T_3 \rangle$ ), respectively. Owing to the larger SOC effect between  $T_2/T_3$  state and  $S_1$  state, PT-1 can capture triplet excitons more effectively,<sup>[16]</sup> thereby exhibiting an outstanding electroluminescence performance.<sup>[17]</sup> Consequently, although the photophysical behaviors of the two molecules are fully similar, there are fundamental differences in the mechanisms of exciton production between light pump irradiation and electron-hole pairs injected. The above results indicate that the construction of high-energy level triplet states has an important influence on the trapping ability of triplet excitons.

## 2.6. PhOLEDs based on PT-1 as host

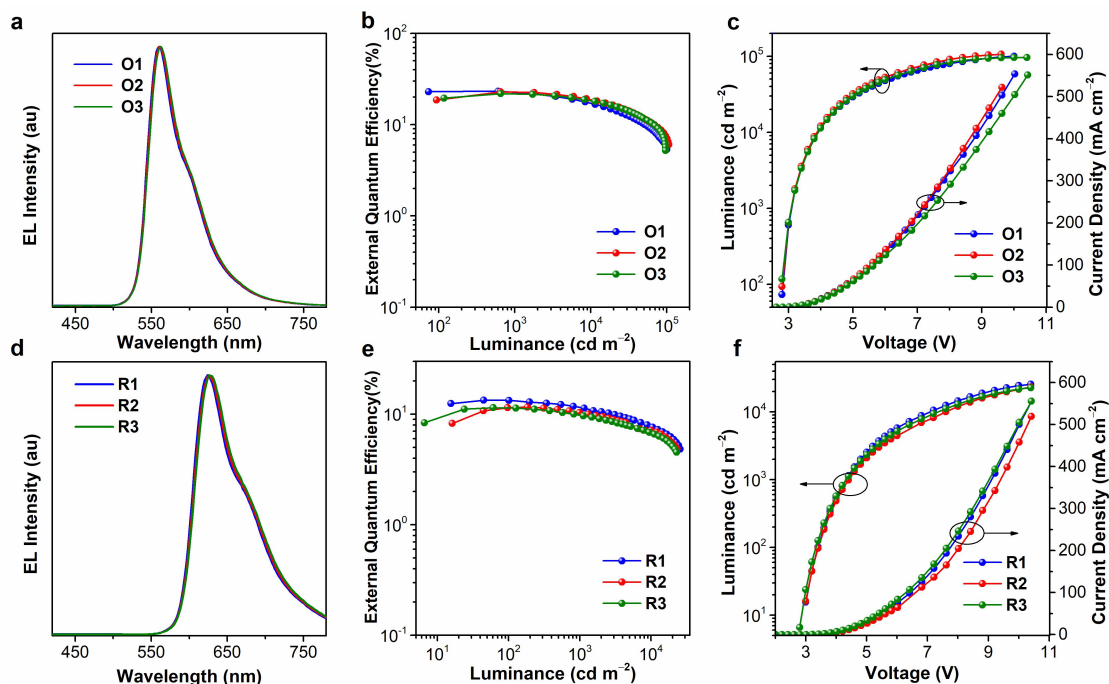


**Figure 4.** (a) EL spectra, (b) external quantum efficiency–luminance curves, and (c) luminance–voltage–current density plots of orange PhOLEDs employing PT-1 as host. (d) EL spectra, (e) external quantum efficiency–luminance curves, and (f) luminance–voltage–current density plots of red PhOLEDs employing PT-1 as host.

**Table 3.** EL performances of PhOLEDs based on PT-1 as hosts.

EML	Device	$\lambda_{\text{EL}}^{[\text{a}]}$	$V_{\text{on}}^{[\text{b}]}$	$L^{[\text{c}]}$	$\eta_{\text{c}}^{[\text{c}]}$	$\eta_{\text{p}}^{[\text{c}]}$	$\eta_{\text{ext}}^{[\text{c}]}$	CIE (x, y) <sup>[d]</sup>
		[nm]	[V]	[cd m <sup>-2</sup> ]	[cd A <sup>-1</sup> ]	[lm W <sup>-1</sup> ]	[%]	
ITO/HATCN (5 nm)/TAPC (50 nm)/TCTA (5 nm)/EML (20 nm)/TPBi (40 nm)/LiF (1 nm)/Al (120 nm)								
PT-1: 3 wt% PO-01-TB	O1	560	2.7	99950	79.41	87.88	23.28	(0.47, 0.52)
PT-1: 5 wt% PO-01-TB	O2	560	2.7	106200	77.34	80.99	22.91	(0.48, 0.52)
PT-1: 8 wt% PO-01-TB	O3	562	2.7	96110	73.08	76.53	21.89	(0.48, 0.51)
PT-1: 3 wt% Ir(piq) <sub>2</sub> acac	R1	623	3.0	25560	11.17	10.93	13.37	(0.67, 0.32)
PT-1: 5 wt% Ir(piq) <sub>2</sub> acac	R2	624	3.0	23270	9.28	8.10	11.60	(0.68, 0.32)
PT-1: 8 wt% Ir(piq) <sub>2</sub> acac	R3	625	2.8	22760	8.79	8.63	11.46	(0.68, 0.32)

<sup>[a]</sup> $\lambda_{\text{EL}}$  = EL maximum. <sup>[b]</sup> $V_{\text{on}}$  = turn-on voltage at 1 cd m<sup>-2</sup>. <sup>[c]</sup>The luminescence ( $L$ ), current efficiency ( $\eta_c$ ), power efficiency ( $\eta_p$ ), external quantum efficiency ( $\eta_{\text{ext}}$ ) are the maximum values of the devices. <sup>[d]</sup>CIE = Commission Internationale de L'Eclairage, recorded at 10 mA cm<sup>-2</sup>.

In addition, PT-1 was employed as the host for phosphorescent materials to explore its potential further. As shown in Figure 4, PhOLEDs were fabricated with a device configuration of ITO/HATCN (5 nm)/TAPC (50 nm)/TCTA (5 nm)/ EML (20 nm)/TPBi (40 nm)/LiF (1 nm)/Al (120 nm), where the EMLs are PT-1: x wt% (x = 3, 5, and 8) PO-01-TB for devices O1-3 and x wt% (x = 3, 5, and 8) Ir(piq)<sub>2</sub>acac for device R1-3. The absorption of PO-01-TB and Ir(piq)<sub>2</sub>acac exhibited good spectral overlap with the emission of PT-1 (Figure S10), indicating that efficient Förster resonance energy transfer (FRET) from the host to the guest unit can be expected. The turn-on voltage of these devices is 2.7 eV, which indicates that holes and electrons can be easily injected into EML. This could be attributed to the reasonable energy level matching between PT-1 and each functional layer. All the devices only emit orange light from PO-01-TB, which confirms an efficient energy transfer from the host to the guest in the EL process. As summarized in Table 3, the high-performance orange phosphorescent devices are obtained with phosphorescent guest materials doped at a concentration of 3%, with maximum  $L_{\max}$ ,  $\eta_c$ ,  $\eta_p$ , and  $\eta_{\text{ext}}$  of 99950 cd m<sup>-2</sup>, 79.41 cd A<sup>-1</sup>, 87.88 lm W<sup>-1</sup>, and 23.28%, respectively. Furthermore, the device can still maintain excellent device performance at 1000 cd m<sup>-2</sup>, with  $\eta_c$ ,  $\eta_p$ , and  $\eta_{\text{ext}}$  of 74.52 cd A<sup>-1</sup>, 73.16 lm W<sup>-1</sup>, and 21.83%, respectively, indicating of small efficiency roll-off and good efficiency stability. Moreover, device R1 exhibits stable performance in red PhOLEDs, the maximum  $\eta_{\text{ext}}$  and  $\eta_p$  are 13.37% and 10.93 lm W<sup>-1</sup>, respectively, and the device still maintains  $\eta_{\text{ext}}$  and  $\eta_p$  of 11.79% and 7.45 lm W<sup>-1</sup> at 1000 cd m<sup>-2</sup>. The reason for the lower efficiency of red phosphorescent devices may be attributed to the energy gap law.<sup>[18]</sup> The Ir(piq)<sub>2</sub>acac with a significantly narrow band gap has a high non-radiative decay rate ( $k_{\text{nr}}$ ), resulting in the loss of part of the energy in a



nonradiative channel. Additionally, to better understand the emission mechanism in these devices, a diagram of the energy transfer process based on the HLCT emitter is shown in Figure S11. As holes and electron carriers are injected into the EML, carriers first form polarons and then excitons mainly on the host. The hRISC channels from  $T_2/T_3$  to  $S_1$  mainly take place on the PT-1 molecule with HLCT character, which makes more effective utilization of the triplet excitons. Subsequently, the long-wavelength phosphorescent guest was excited through FRET.<sup>[19]</sup> Owing to the reduction in the DET process from the host to the guest, the TTA effect was suppressed. These results eventually make the dopant emitters sensitized effectively, and the efficiency of the devices exhibited low roll-off.

## 2.7. Two-Color Hybrid WOLEDs

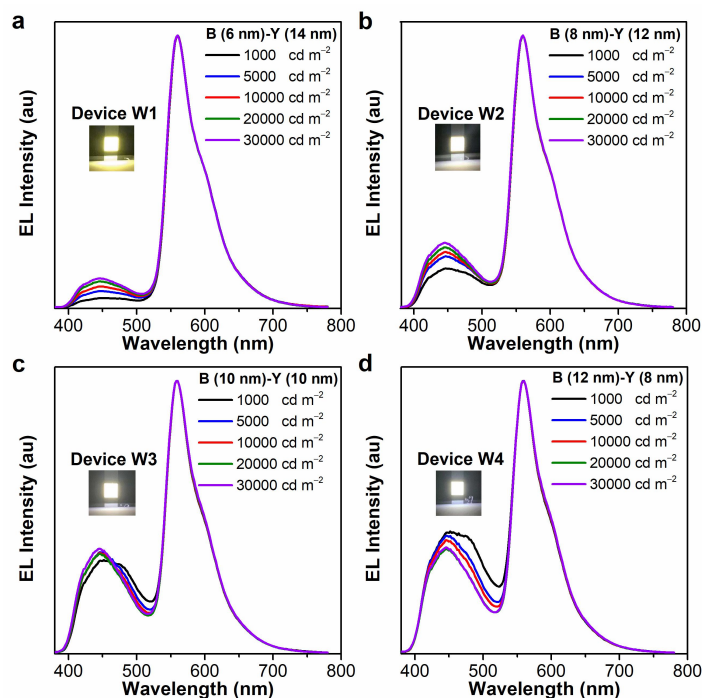


**Figure 5.** EL spectra of WOLEDs at varied luminance, (a) - (d) correspond to devices W1 - W4, respectively.

**Table 4.** EL performances of two-color hybrid WOLEDs based on PT-1.

Device	$V_{on}^{[b]}$ [V]	$L^{[c]}$ [cd m <sup>-2</sup> ]	$\eta_c^{[c]}$ [cd A <sup>-1</sup> ]	$\eta_p^{[c]}$ [lm W <sup>-1</sup> ]	$\eta_{ext}^{[c]} \max / @1000 \text{ cd m}^{-2}$ / / $@5000 \text{ cd m}^{-2}$ [%]	CRI	CIE (x, y) <sup>[d]</sup>
--------	-----------------------	------------------------------------	---	---	---	-----	---------------------------

W1	2.8	95280	80.56	84.37	23.93 / 22.24 / 17.34	34	(0.45, 0.49)
W2	2.8	73520	64.58	67.63	19.82 / 15.9 / 12.40	40	(0.41, 0.45)
W3	2.8	62590	36.79	38.53	12.32 / 10.27 / 8.94	50	(0.36, 0.39)
W4	2.8	66200	30.27	33.96	10.49 / 9.41 / 8.61	55	(0.34, 0.37)

$V_{\text{on}}$  = turn on voltage at  $1 \text{ cd m}^{-2}$ ;  $L_{\text{max}}$  = maximum luminance;  $\eta_{\text{c}}$  = current efficiency;  $\eta_{\text{p}}$  = power efficiency;  $\eta_{\text{ext}}$  = external quantum efficiency; CIE coordinates at  $1000 \text{ cd m}^{-2}$ ; CRI = color rendering index.

In view of the above results, PT-1 with HLCT character exhibits excellent multifunctionality in non-doped devices and the host material of PhOLEDs. Therefore, PT-1 with deep-blue emission was further used to fabricate two-color hybrid WOLEDs (Figure 5) with a configuration of ITO/HATCN (5 nm)/TAPC (50 nm)/TcTa (5 nm)/PT-1 (B nm)/PT-1: 3 wt% PO-01-TB (Y nm)/TPBi (40 nm)/LiF (1 nm)/Al (120 nm) without any interlayers, where the neat film of PT-1 was used as a deep-blue EML and the layer of PT-1: 3 wt% PO-01-TB is used as an orange emitting layer. Devices W1-4 corresponds to 14, 12, 10, and 8 nm of the thickness of the orange emitting layer. As summarized in Table 4, the two-color hybrid WOLEDs all show a lower turn-on voltage of 2.8 V. Device W1 shows excellent warm-white light emission, and the values of  $\eta_{\text{c,max}}$ ,  $\eta_{\text{p,max}}$ , and  $\eta_{\text{ext,max}}$  are  $80.56 \text{ cd A}^{-1}$ ,  $84.37 \text{ lm W}^{-1}$  and 23.93%, respectively. Moreover, device W1 can maintain EQE and PE of 22.24% and  $74.66 \text{ lm W}^{-1}$  at  $1000 \text{ cd m}^{-2}$ , respectively, exhibiting a high EQE level and small efficiency roll-off under practical lighting luminance. In addition to the change in the thickness of the phosphorescence layer (device W1 to W4), these devices can realize the transformation from warm white to quasi-white light. Device W4 (Y = 8 nm) shows excellent quasi-white light emission at CIE coordinates of (0.34, 0.37), and the values of  $\eta_{\text{c,max}}$ ,  $\eta_{\text{p,max}}$ , and  $\eta_{\text{ext,max}}$  are  $20.27 \text{ cd A}^{-1}$ ,  $33.96 \text{ lm W}^{-1}$ , and 10.48%, respectively. These high-performance

electroluminescent devices can be attributed to the reasonable energy level matching with each functional layer; thus, whether PT-1 is used as the host of phosphorescent material or the deep-blue light-emitting layer, the holes and electrons can be easily injected into the EML. In addition, as mentioned in Section 2.6, through the efficient hRISC and FRET processes in the orange emitting layer, the exciton loss caused by TTA is effectively reduced.

### 3. Conclusion

In summary, PT-1 and PT-2 were synthesized and fully characterized. Owing to the fundamentally identical electronic configuration of the  $S_1$  state, the photoluminescence behaviors of the two molecules are similar. However, the NTOs of the  $T_2$  and  $T_3$  states, which border the energy level of the  $S_1$  state, have partially different distributions on the triazole. In addition, the SOC values are quite different for the two molecules, which lead to PT-1 possessing a better excellent electroluminescence performance. The non-doped OLED based on PT-1 exhibits an  $\eta_{\text{ext,max}}$  of 6.63% with a low efficiency roll-off. Moreover, the host of PhOLEDs and blue emitting layer in two-color hybrid WOLEDs based on PT-1 have been constructed and they have achieved outstanding performance. Two-color hybrid WOLEDs can realize the transformation from warm-white to quasi-white light via tuning the thickness of emission layer, with maximum  $\eta_{\text{ext}}$  and  $\eta_{\text{p}}$  of 23.93% / 84.37 lm W<sup>-1</sup> and 10.49% / 33.96 lm W<sup>-1</sup>, respectively. In conclusion, these results indicate that the characteristics of high-lying excited states are particularly crucial for electroluminescence, promote research on the characteristic regulation of high-lying excited states, and inspire the development of high-performance WOLEDs.

**Supporting Information**

Supporting Information is available from the Wiley Online Library or from the author.

**Acknowledgements**

We are grateful for financial support from the National Natural Science Foundation of China (21788102 and 21975077), National Key R&D Program of China (Intergovernmental cooperation project, 2017YFE0132200), Open Research Project of Military Logistics Support Department (BLB19J008), the Fundamental Research Funds for the Central Universities (2019ZD04), Natural Science Foundation of Guangdong Province (2020A1515011542) and Fund of Guangdong Provincial Key Laboratory of Luminescence from Molecular Aggregates (2019B030301003).

**Conflict of Interest**

The authors declare no conflict of interest.

Received: ((will be filled in by the editorial staff))

Revised: ((will be filled in by the editorial staff))

Published online: ((will be filled in by the editorial staff))

**References**

- [1] C. W. Tang, S. A. VanSlyke, *Appl. Phys. Lett.* **1987**, *51*, 913.
- [2] a) J. Kido, M. Kimura, K. Nagai, *Science* **1995**, *267*, 1332; b) M. Zhu, C. Yang, *Chem. Soc. Rev.* **2013**, *42*, 4963; c) Z. Xu, B. Z. Tang, Y. Wang, D. Ma, *J. Mater. Chem. C* **2020**, *8*, 2614.
- [3] a) D. D. Zhang, L. Duan, *Nat. Photon.* **2021**, *15*, 173; b) D. Wang, C. Cheng, T. Tsuboi, Q. Zhang, *CCS Chem.* **2020**, *2*, 1278.
- [4] a) X. F. Qiao, D. G. Ma, *Mat. Sci. Eng. R.* **2020**, *139*, 38; b) C. Murawski, K. Leo, M. C. Gather, *Adv. Mater.* **2013**, *25*, 6801; c) J. Jortner, S. A. Rice, J. L. Katz, S. I. Choi, *J. Chem. Phys.* **1965**, *42*, 309.
- [5] a) H. Uoyama, K. Goushi, K. Shizu, H. Nomura, C. Adachi, *Nature* **2012**, *492*, 234; b) Q. Zhang, B. Li, S. Huang, H. Nomura, H. Tanaka, C. Adachi, *Nat. Photon.* **2014**, *8*, 326; c) Y. Liu, C. Li, Z. Ren, S. Yan, M. R. Bryce, *Nat. Rev. Mater.* **2018**, *3*, 1.

- [6] a) H. Noda, X. K. Chen, H. Nakanotani, T. Hosokai, M. Miyajima, N. Notsuka, Y. Kashima, J. L. Bredas, C. Adachi, *Nat. Mater.* **2019**, *18*, 1084; b) X.-K. Chen, S.-F. Zhang, J.-X. Fan, A.-M. Ren, *J. Phys. Chem. C* **2015**, *119*, 9728; c) W. Li, M. Li, W. Li, Z. Xu, L. Gan, K. Liu, N. Zheng, C. Ning, D. Chen, Y. C. Wu, S. J. Su, *ACS Appl. Mater. Interfaces* **2021**, *13*, 5302.
- [7] a) Y. Xu, X. Liang, X. Zhou, P. Yuan, J. Zhou, C. Wang, B. Li, D. Hu, X. Qiao, X. Jiang, *Adv. Mater.* **2019**, *31*, 1807388; b) Y. Xu, C. Wang, X. Zhou, J. Zhou, X. Guo, X. Liang, D. Hu, F. Li, D. Ma, Y. Ma, *J. Phys. Chem. Lett.* **2019**, *10*, 6878; c) X. Lv, L. Xu, M. Cang, R. Wang, M. Sun, H. Zhou, Y. Yu, Q. Sun, Y. Pan, Y. Xu, *CCS Chem.* **2020**, *2*, 2557.
- [8] a) H. Zhang, A. Li, G. Li, B. Li, Z. Wang, S. Xu, W. Xu, B. Z. Tang, *Adv. Opt. Mater.* **2020**, *8*, 1902195; b) X. Tang, R. Pan, X. Zhao, H. Zhu, Z. Xiong, *J. Phys. Chem. Lett.* **2020**, *11*, 2804; c) Y. Xu, P. Xu, D. Hu, Y. Ma, *Chem. Soc. Rev.* **2021**, *50*, 1030.
- [9] X. Tang, Q. Bai, T. Shan, J. Li, Y. Gao, F. Liu, H. Liu, Q. Peng, B. Yang, F. Li, P. Lu, *Adv. Funct. Mater.* **2018**, *28*, 1705813.
- [10] a) Z. R. Grabowski, K. Rotkiewicz, W. Rettig, *Chem. Rev.* **2003**, *103*, 3899; b) S. Zhang, L. Yao, Q. Peng, W. Li, Y. Pan, R. Xiao, Y. Gao, C. Gu, Z. Wang, P. Lu, F. Li, S. Su, B. Yang, Y. Ma, *Adv. Funct. Mater.* **2015**, *25*, 1755.
- [11] Z. R. Grabowski, K. Rotkiewicz, W. Rettig, *Chem. Rev.* **2003**, *103*, 3899.
- [12] M. A. Baldo, D. O'brien, M. Thompson, S. Forrest, *Phys. Rev. B* **1999**, *60*, 14422.
- [13] X. Tang, R. Pan, X. Zhao, W. Jia, Y. Wang, C. Ma, L. Tu, Z. Xiong, *Adv. Funct. Mater.* **2020**, *30*, 2005765.

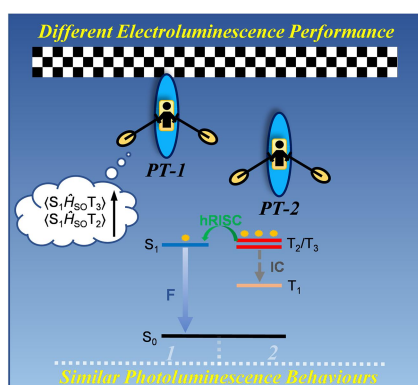
- [14] a) A. P. Demchenko, V. I. Tomin, P.-T. Chou, *Chem. Rev.* **2017**, *117*, 13353; b) L. Yao, S. Zhang, R. Wang, W. Li, F. Shen, B. Yang, Y. Ma, *Angew. Chem. Int. Ed. Engl.* **2014**, *53*, 2119.
- [15] D. Hu, L. Yao, B. Yang, Y. Ma, *Phil. Trans. R. Soc. A* **2015**, *373*, 20140318.
- [16] V. Lawetz, G. Orlandi, W. Siebrand, *J. Chem. Phys.* **1972**, *56*, 4058.
- [17] H. Zhang, B. Zhang, Y. Zhang, Z. Xu, H. Wu, P. A. Yin, Z. Wang, Z. Zhao, D. Ma, B. Z. Tang, *Adv. Funct. Mater.* **2020**, *30*, 2002323.
- [18] a) R. Englman, J. Jortner, *Mol. Phys.* **1970**, *18*, 145. b) J. S. Wilson, N. Chawdhury, M. R. A. Al-Mandhary, M. Younus, M. S. Khan, P. R. Raithby, A. Köhler, R. H. Friend, *J. Am. Chem. Soc.* **2001**, *123*, 9412. c) U. Balijapalli, R. Nagata, N. Yamada, H. Nakanotani, M. Tanaka, A. D'Aléo, V. Placide, M. Mamada, Y. Tsuchiya, C. Adachi, *Angew. Chem. Int. Ed. Engl.* **2021**, *60*, 8477.
- [19] a) H. Zhang, J. Xue, C. Li, S. Zhang, B. Yang, Y. Liu, Y. Wang, *Adv. Funct. Mater.* **2021**, *31*, 2100704; b) X. Ouyang, X.-L. Li, L. Ai, D. Mi, Z. Ge, S.-J. Su, *ACS Appl. Mater. Interfaces* **2015**, *7*, 7869; c) X. Ouyang, X.-L. Li, Y. Bai, D. Mi, Z. Ge, S.-J. Su, *RSC Adv.* **2015**, *5*, 32298.

Two novel molecules with deep-blue emission, PT-1 and PT-2, exhibit the nearly identical photophysical behaviour. However, due to the larger SOC effect between  $T_2/T_3$  state and  $S_1$  state for PT-1, triplet excitons can be captured more effectively, thereby exhibiting an outstanding electroluminescence performance.

*Baoxi Li, Gangang Li, Han Zhang, Haozhong Wu, Kongqi Chen, Zhiming Wang\*, and Ben Zhong Tang\**

## Critical Role of High-lying Triplet States for Efficient Excitons Utilization in High-Performance Non-doped Deep-blue Fluorescent and Hybrid White Organic Light-Emitting Diodes

### Table of Contents



## Supporting Information

### **Critical Role of High-lying Triplet States for Efficient Excitons Utilization in High-Performance Non-doped Deep-blue Fluorescent and Hybrid White OLEDs**

*Baoxi Li, Ganggang Li, Han Zhang, Haozhong Wu, Kongqi Chen, Zhiming Wang\*, and Ben Zhong Tang\**

#### **Contents**

- 1. General Information**
- 2. Experimental Section**
- 3. Computational Methods**
- 4. Device fabrication and measurement**
- 5. Reference**

#### **1. General Information**

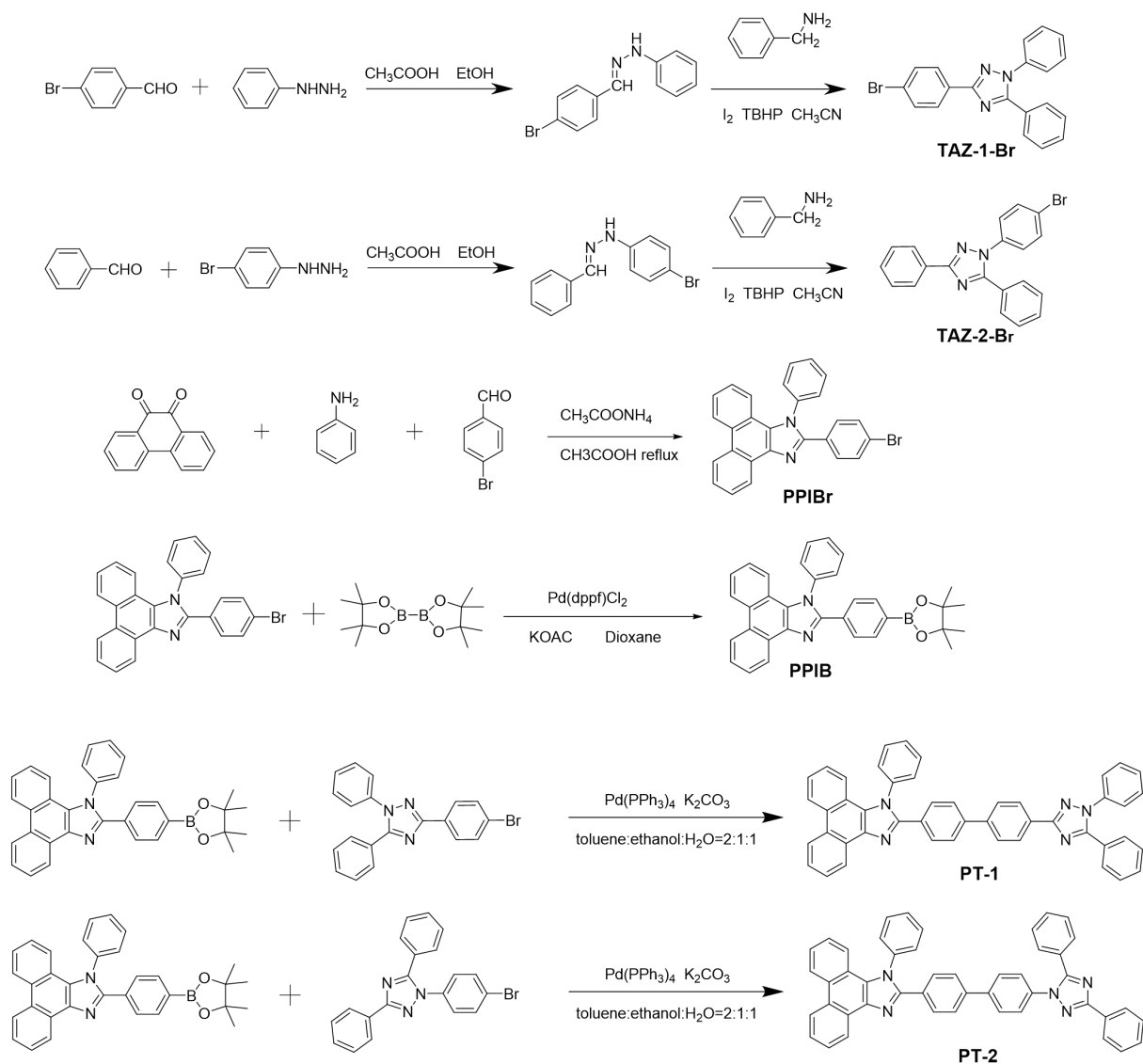
All the reagents and solvents were purchased from commercial sources and used as received. without further purification. The final products were subjected to vacuum sublimation to further improve purity before photoluminescence (PL) and electroluminescence (EL) properties investigations.  $^1\text{H}$  and  $^{13}\text{C}$  NMR spectra were recorded on a Bruker AV 500 spectrometer in appropriated deuterated dichloromethane or trichloromethane at room temperature. High resolution mass spectra (HRMS) were tested on Agilent1290/Bruker maXis impact. Thermogravimetric analysis (TGA) was performed on a TA TGA Q5000 from 30 °C



to 800 °C under dry nitrogen at a heating rate of 10 °C min<sup>-1</sup>. The differential scanning calorimetry (DSC) analysis was carried out on a DSC Q1000 from 30 °C to 350 °C under dry nitrogen at a heating rate of 10 °C min<sup>-1</sup>. Cyclic voltammetry (CV) was measured on a CHI 610E A14297 in a solution of tetra-*n*-butylammonium hexafluorophosphate (Bu<sub>4</sub>NPF<sub>6</sub>) (0.1 M) in dichloromethane or dimethylformamide at a scan rate of 100 mV s<sup>-1</sup>, using a platinum wire as the auxiliary electrode, a glass carbon disk as the working electrode and Ag/Ag<sup>+</sup> as the reference electrode, the calibrated value was performed by the redox couple ferricenium/ferrocene (Fc/Fc<sup>+</sup>). The Ionization Potential (IP<sub>CV</sub>) and Electron Affinities (EA<sub>CV</sub>) of these molecules were calculated by the following formula, Ionization Potential (IP<sub>CV</sub>) =  $[E_{\text{ox}} - E_{1/2}(\text{Fc}/\text{Fc}^+) + 4.8]$  eV, Electron Affinities (EA<sub>CV</sub>) =  $[E_{\text{red}} - E_{1/2}(\text{Fc}/\text{Fc}^+) + 4.8]$  eV, where  $E_{\text{ox}}$  and  $E_{\text{red}}$  represents the onset oxidation potential and the reduction potential relative to Fc/Fc<sup>+</sup> (4.8 eV), respectively. UV-vis absorption spectra were measured on Shimadzu UV-2600 spectrophotometer. Measurements of PL spectra were performed on Horiba Fluoromax-4 spectrofluorometer. Fluorescence quantum yields of solutions and solid films were measured by using a Hamamatsu absolute PL quantum yield spectrometer C11347 Quantaaurus QY. Fluorescence lifetimes were determined on a Hamamatsu C1136711 Quantaaurus-Tau time-resolved spectrometer.

## 2. Experimental Section

### 2.1 Synthesis and characterization



**Scheme S1.** Molecular structures and synthetic routes of the PT-1 and PT-2.

**3-(4-bromophenyl)-1,5-diphenyl-1H-1,2,4-triazole (TAZ-1-Br):** 4-Bromobenzaldehyde (1.85 g, 10 mmol), and Phenylhydrazine (1.08 g, 10 mmol) were mixed into ethanol (100 ml) of round bottom flask, refluxed for 3 h to obtain the hydrazone; Subsequently, the precipitated hydrazone was filtered, washed and dried. The further purification was carried out by recrystallization in ethanol. Then the purified hydrazone (2.75 g, 10 mmol), Benzylamine (3.21 g, 30 mmol), I<sub>2</sub> (20 mol %) and TBHP (70% aq. 30 mmol) were put into acetonitrile (90 mL), heated and refluxed for 8 h. As the reaction cooled to room temperature, the mixture was

poured into the solution of water and extracted with dichloromethane for several times. The extract was washed with 10% Na<sub>2</sub>S<sub>2</sub>O<sub>3</sub> solution, dried over anhydrous MgSO<sub>4</sub> and evaporated under reduced pressure to obtain the crude product, which was purified by silica gel column chromatography (petroleum ether/DCM, 4:1). White solid of **TAZ-1-Br** was obtained in 75% yield. <sup>1</sup>H NMR (500 MHz, CDCl<sub>3</sub>),  $\delta$  (TMS, ppm): 8.13 (d, J = 8.5 Hz, 2H), 7.60 (d, J = 8.5 Hz, 2H), 7.54 (dd, J = 13.3, 11.9 Hz, 2H), 7.48 – 7.40 (m, 6H), 7.37 (t, J = 7.4 Hz, 2H). <sup>13</sup>C NMR (125 MHz, CDCl<sub>3</sub>),  $\delta$  (TMS, ppm): 160.86, 154.82, 138.10, 131.81, 130.27, 129.49, 129.04, 128.67, 128.23, 127.53, 125.41, 123.80. HRMS (C<sub>20</sub>H<sub>14</sub>BrN<sub>3</sub>): m/z 376.0448 (M<sup>+</sup>, calcd 376.0444).

**1-(4-bromophenyl)-3,5-diphenyl-1H-1,2,4-triazole (TAZ-2-Br):** The synthetic route of the procedure is analogous to that described for **TAZ-1-Br**. Yellow solid, yield 52%. <sup>1</sup>H NMR (500 MHz, CDCl<sub>3</sub>),  $\delta$  (TMS, ppm): 8.22 (d, J = 6.8 Hz, 2H), 7.59 – 7.52 (m, 4H), 7.49 – 7.36 (m, 6H), 7.34 – 7.28 (m, 2H). <sup>13</sup>C NMR (125 MHz, CDCl<sub>3</sub>),  $\delta$  (TMS, ppm): 162.18, 154.80, 137.26, 132.55, 130.50, 130.25, 129.55, 128.99, 128.69, 127.79, 126.67, 122.54. HRMS (C<sub>20</sub>H<sub>14</sub>BrN<sub>3</sub>): m/z 376.0448 (M<sup>+</sup>, calcd 376.0444).

**1-phenyl-2-(4-(4,4,5,5-tetramethyl-1,3,2-dioxaborolan-2-yl)phenyl)-1H-phenanthro[9,10-d]imidazole (PPIB):** A mixture of compound **PPIBr** (1.348 g, 3 mmol), bis(pinacolato)diboron (1.143 g, 4.5 mmol, 1.5 equiv), KOAc (0.88 g, 9 mmol, 3 equiv), Pd(dppf)Cl<sub>2</sub> (0.54 g, 0.66 mmol, 0.03 equiv) were placed in a 100 mL round bottom flask under nitrogen. Then 60 ml dioxane was injected into the bottle, and the reaction mixture refluxed for 24 h. As the reaction cooled to room temperature, the mixture was poured into the solution of water and extracted with dichloromethane for several times. The extract dried over

anhydrous MgSO<sub>4</sub> and evaporated under reduced pressure to obtain the crude product, which was purified by silica gel column chromatography (petroleum ether/DCM, 1:1). White solid of **PPIB** was obtained in 85% yield. <sup>1</sup>H NMR (500 MHz, CDCl<sub>3</sub>),  $\delta$  (TMS, ppm): 8.89 (d, *J* = 7.6 Hz, 1H), 8.77 (d, *J* = 8.2 Hz, 1H), 8.70 (d, *J* = 8.3 Hz, 1H), 7.80 – 7.44 (m, 12H), 7.26 (m, *J* = 6.3 Hz, 1H), 7.18 (d, *J* = 7.7 Hz, 1H), 1.34 (d, *J* = 1.9 Hz, 12H). <sup>13</sup>C NMR (125 MHz, CDCl<sub>3</sub>),  $\delta$  (TMS, ppm): 150.72, 138.72, 137.47, 134.49, 132.90, 130.15, 129.78, 129.34, 129.10, 128.56, 128.27, 127.24, 126.26, 125.65, 124.94, 124.10, 123.06, 122.82, 120.91, 83.94, 24.90. HRMS (C<sub>33</sub>H<sub>29</sub>BN<sub>2</sub>O<sub>2</sub>): *m/z* 497.2414 (M<sup>+</sup>, calcd 497.2401).

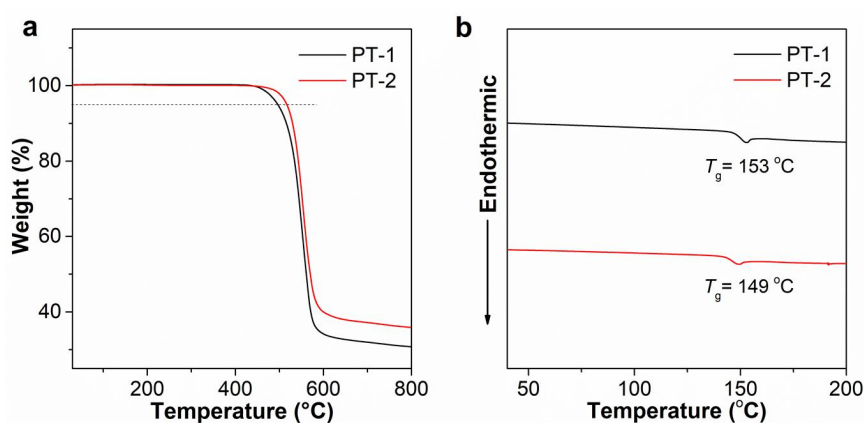
**2-(4'-(1,5-diphenyl-1H-1,2,4-triazol-3-yl)-[1,1'-biphenyl]-4-yl)-1-phenyl-1H-phenanthro[9,10-d]imidazole (PT-1):** **PPIB** (1.123g, 2.5 mmol), **TAZ-1-Br** (1.125g, 3 mmol), Pd(PPh<sub>3</sub>)<sub>4</sub> (0.087 g, 0.075 mmol, 0.03 equiv), K<sub>2</sub>CO<sub>3</sub> and (2.0 M, 4.14 g) was placed in 100 mL round bottom flask under nitrogen. Then, a mixed solvent system of 30mL toluene, 15mL ethanol and 15mL H<sub>2</sub>O was injected into the bottle, and the reaction mixture refluxed for 24 h. As the reaction cooled to room temperature, the mixture was poured into the solution of water and extracted with dichloromethane for several times. The extract dried over anhydrous MgSO<sub>4</sub> and evaporated under reduced pressure to obtain the crude product, which was purified by silica gel column chromatography (petroleum ether/DCM, 1:1). White solid of **PT-1** was obtained in 89% yield. <sup>1</sup>H NMR (500 MHz, CD<sub>2</sub>Cl<sub>2</sub>),  $\delta$  (TMS, ppm): 8.92 (d, *J* = 7.8 Hz, 1H), 8.78 (d, *J* = 8.3 Hz, 1H), 8.72 (d, *J* = 8.3 Hz, 1H), 8.31 (d, *J* = 8.3 Hz, 2H), 7.76 (t, *J* = 7.3 Hz, 1H), 7.73 – 7.47 (m, 15H), 7.47 – 7.33 (m, 8H), 7.27 (d, *J* = 6.0 Hz, 1H), 7.20 (d, *J* = 7.8 Hz, 1H). <sup>13</sup>C NMR (125 MHz, CDCl<sub>3</sub>),  $\delta$  (TMS, ppm): 161.60, 154.84, 150.51, 141.01, 140.78, 138.80, 138.27, 137.45, 130.25, 129.97, 129.73, 129.51 – 128.77, 128.61, 128.27, 127.98,

127.31, 127.09, 126.76, 126.28, 125.65, 125.44, 124.91, 124.12, 123.07, 122.83, 120.88.

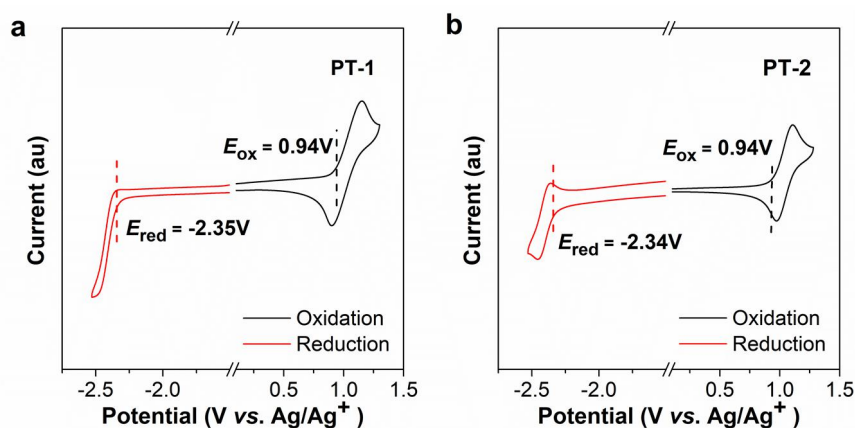
HRMS ( $C_{47}H_{31}N_5$ ):  $m/z$  666.2666 ( $M^+$ , calcd 666.2652).

**2-(4'-(3,5-diphenyl-1H-1,2,4-triazol-1-yl)-[1,1'-biphenyl]-4-yl)-1-phenyl-1H-phenanthro[9,10-d]imidazole (PT-2):** The synthetic route of the procedure is analogous to that described for **PT-1**. White solid, yield 88%.  $^1H$  NMR (500 MHz,  $CDCl_3$ ),  $\delta$  (TMS, ppm):

8.90 (d,  $J = 7.8$  Hz, 1H), 8.77 (d,  $J = 8.3$  Hz, 1H), 8.71 (d,  $J = 8.3$  Hz, 1H), 8.30 – 8.18 (m, 2H), 7.76 (t,  $J = 7.4$  Hz, 1H), 7.72 – 7.33 (m, 23H), 7.30 – 7.25 (d, 1H), 7.19 (d,  $J = 8.0$  Hz, 1H).  $^{13}C$  NMR (125 MHz,  $CDCl_3$ ),  $\delta$  (TMS, ppm): 162.05, 154.77, 150.21, 140.61, 139.81, 138.76, 137.61, 130.69, 130.29, 130.19 – 129.73, 129.40, 129.09, 128.64, 128.32, 128.06, 127.85, 127.35, 126.84, 126.62, 126.32, 125.65, 125.00, 124.15, 123.14, 122.98, 122.78, 120.87. HRMS ( $C_{47}H_{31}N_5$ ):  $m/z$  666.2668 ( $M^+$ , calcd 666.2652).



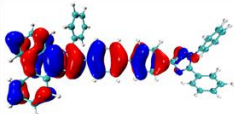
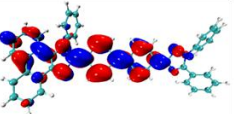
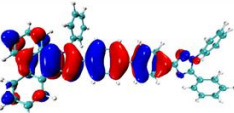
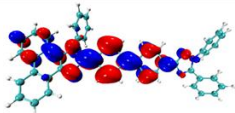
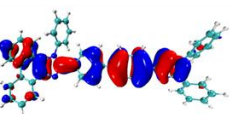
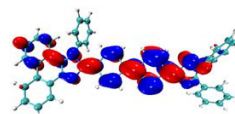
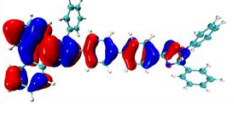
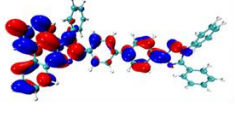
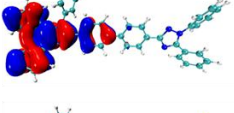
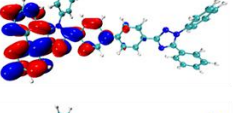
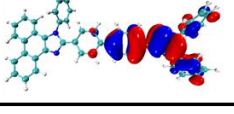
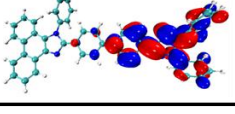
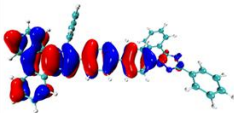
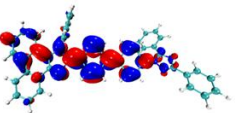
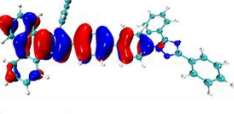
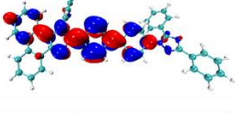
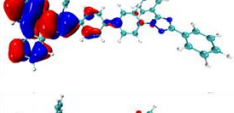
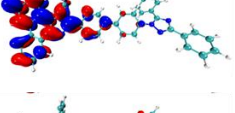
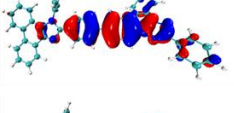
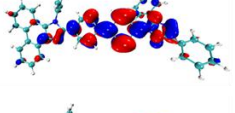
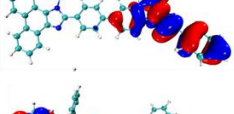
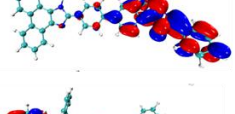
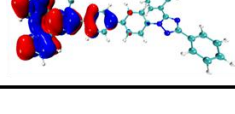
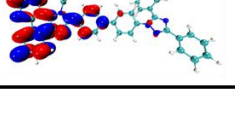
**Figure S1.** (a) Thermogravimetric analysis and (b) differential scanning calorimetry curves of PT-1 and PT-2.



**Figure S2.** Cyclic voltammogram of (a) PT-1 and (b) PT-2.

### 3. Computational Methods

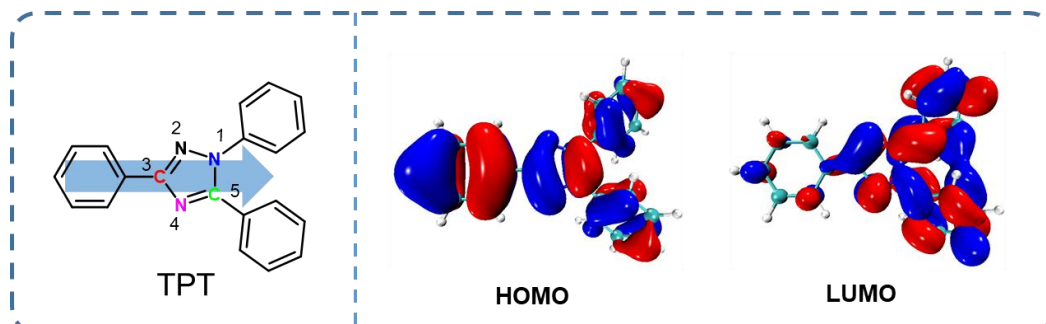
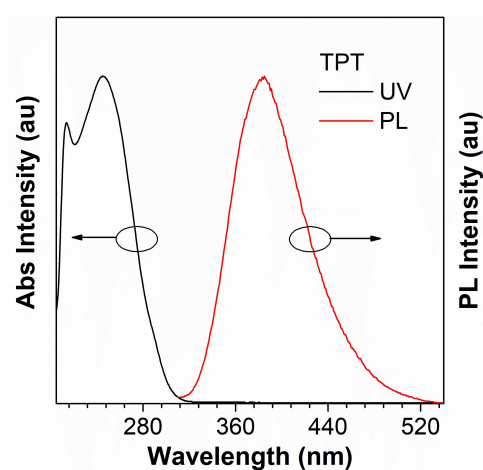
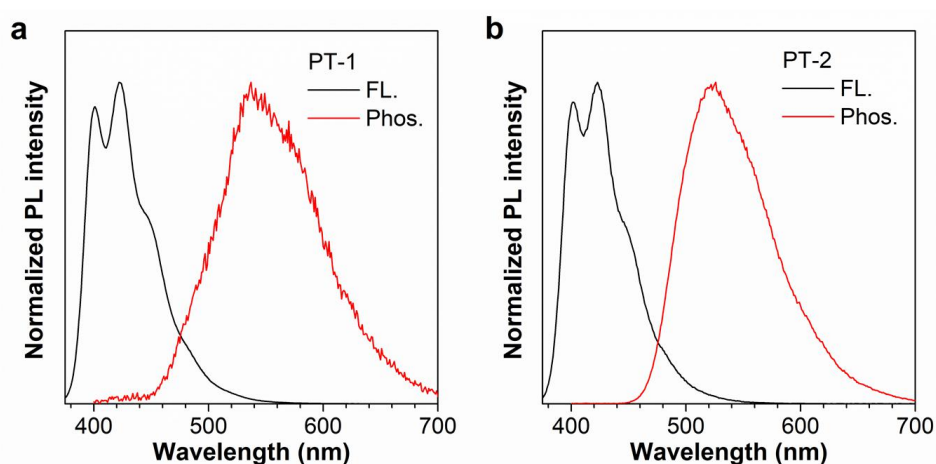
All density functional theory (DFT) calculations were carried out using Gaussian 16 package. The ground-state (S0) geometries in the gas phase were optimized at the level of B3LYP/6–31G (d, p), a commonly used level for the precise geometry optimization. Geometry optimization of S1, and excited-state properties based on S1 geometries were studied by time-dependent DFT (TDDFT) using M062X/6–31G (d, p) with long-range correction. The NTOs were carried out using Multiwfn that an electron wave function analysis software.<sup>[1]</sup> The spin-orbit coupling was calculated under the Spin-orbit mean-field (SOMF)<sup>[2]</sup> method in conjunction with the RIJCOSX method<sup>[3,4]</sup> to save calculation expense in ORCA Package, and all used functional and basis sets were consistent with the geometry optimization in Gaussian 16.

PT-1	Hole	Particle	Transition character
S <sub>1</sub>		95.93% 	HLCT
T <sub>1</sub>		92.37% 	HLCT
T <sub>2</sub>		48.29% 	HLCT
		42.91% 	LE
T <sub>3</sub>		44.28% 	LE
		26.40% 	LE
PT-2	Hole	Particle	Transition character
S <sub>1</sub>		95.73% 	HLCT
T <sub>1</sub>		93.37% 	HLCT
T <sub>2</sub>		44.89% 	LE
		43.77% 	HLCT
T <sub>3</sub>		44.48% 	LE
		29.57% 	LE

**Figure S3.** The calculated NTO distributions of and transition characters of PT-1 and PT-2.

**Table S1.** Spin orbit coupling (SOC) values for PT-1 and PT-2.

	$\langle S_1 \hat{H}_{SO} T_1 \rangle$ (cm <sup>-1</sup> )	$\langle S_1 \hat{H}_{SO} T_2 \rangle$ (cm <sup>-1</sup> )	$\langle S_1 \hat{H}_{SO} T_3 \rangle$ (cm <sup>-1</sup> )
PT-1	0.095	0.172	0.244
PT-2	0.044	0.062	0.055

**Figure S4.** The frontier orbital distributions of 1,3,5-triphenyl-1H-1,2,4-triazole (TPT).**Figure S5.** Absorption spectra and PL spectra of TPT in THF solutions (10<sup>-5</sup> M).**Figure S6.** Fluorescence spectra at room temperature and phosphorescence spectra at 77 K of



PT-1 (a) and PT-2 (b) in toluene.

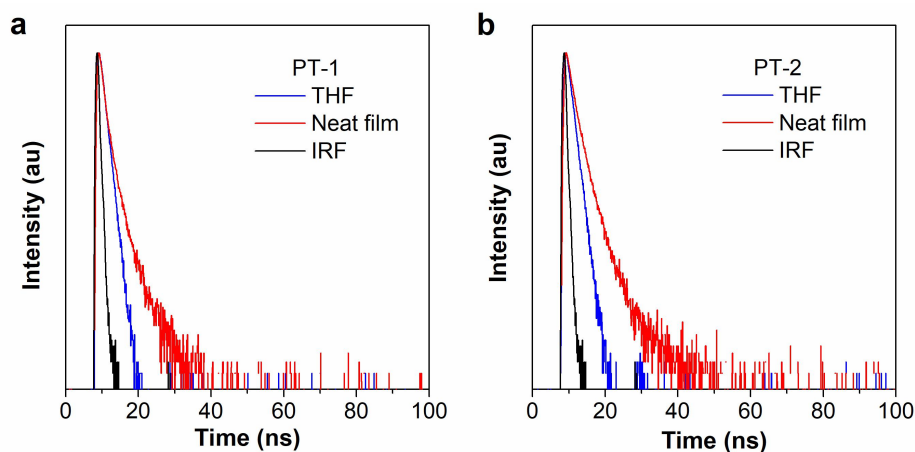


**Figure S7.** Transient decay spectra of (a) PT-1 and (b) PT-2 in THF solutions and vacuum-deposited neat films. IRF: the instrument response function.

### The Lippert-Mataga model

The Lippert-Mataga model <sup>[5]</sup> is estimated according to equation S1

$$hc(v_a - v_f) = hc(v_a^0 - v_f^0) + \frac{2(\mu_e - \mu_g)^2}{a_0^3} f(\epsilon, n) \quad \text{S1}$$

or

$$\mu_e = \mu_g + \left\{ \frac{hca_0^3}{2} \cdot \left[ \frac{d(v_a - v_f)}{df(\epsilon, n)} \right] \right\}^{1/2} \quad \text{S2}$$

where  $\mu_e$  is the dipole moment of excited state,  $\mu_g$  is the dipole moment of ground state,  $h$  is the Plank constant,  $c$  is the light speed in vacuum,  $a_0$  is the solvent Onsager cavity radius,  $v_a - v_f$  is the Stokes shift,  $f(\epsilon, n)$  is the orientational polarizability of solvents and  $f(\epsilon, n) = \left[ \frac{\epsilon-1}{2\epsilon+1} - \frac{n^2-1}{2n^2+1} \right]$ .  $\epsilon$  is the solvent dielectric constant and  $n$  is the solvent refractive index.  $\mu_g$  was estimated by DFT. The differential  $\frac{d(v_a - v_f)}{df(\epsilon, n)}$  can be estimated based on the solvatochromic experiment data.

**Table S2.** Detailed absorption and emission peak positions of PT-1 in different solvents.

PT-1						
Solvents	$\epsilon$	$n$	$f(\epsilon, n)$	$\lambda_a$ (nm)	$\lambda_f$ (nm)	$v_a - v_f$ (cm <sup>-1</sup> )

Hexane	1.9	1.375	0.0012	365	414	3243
Triethylamine	2.42	1.401	0.048	365	417	3416
Butyl ether	3.08	1.399	0.096	365	418	3474
Isopropyl ether	3.88	1.368	0.145	364	417	3492
Ethyl ether	4.34	1.352	0.167	363	418	3625
Tetrahydrofuran	7.58	1.407	0.21	363	422	3852
Dichloromethane	8.93	1.424	0.217	363	427	4129
Dimethyl formamide	37	1.427	0.276	363	432	4400
Acetone	20.7	1.359	0.284	362	427	4205
Acetonitrile	37.5	1.344	0.305	361	435	4712

**Table S3.** Detailed absorption and emission peak positions of PT-2 in different solvents.

PT-2						
Solvents	$\epsilon$	$n$	$f(\epsilon, n)$	$\lambda_a$ (nm)	$\lambda_f$ (nm)	$\nu_a - \nu_f$ (cm <sup>-1</sup> )
Hexane	1.9	1.375	0.0012	364	414	3318
Triethylamine	2.42	1.401	0.048	364	418	3549
Butyl ether	3.08	1.399	0.096	365	419	3531
Isopropyl ether	3.88	1.368	0.145	364	419	3606
Ethyl ether	4.34	1.352	0.167	364	420	3663
Tetrahydrofuran	7.58	1.407	0.21	364	425	3943
Dichloromethane	8.93	1.424	0.217	362	427	4205
Dimethyl formamide	37	1.427	0.276	361	436	4765
Acetone	20.7	1.359	0.284	361	426	4227
Acetonitrile	37.5	1.344	0.305	362	432	4476

#### 4. Device fabrication and measurement

The electroluminescence (EL) devices were fabricated by the vacuum-deposition method. The organic layer passes through a high-vacuum ( $5 \times 10^{-6}$  Torr) onto a glass substrate pre-coated with an indium tin oxide (ITO) layer with a sheet resistance of  $25 \Omega \text{ square}^{-1}$ . The ITO substrates need to be soaked in ultrasonic bath of acetone, isopropanol, detergent, and deionized water respectively for 10 minutes and dried before it can be transferred to the evaporation chamber for making further efforts. The vacuum-deposited OLEDs were fabricated in the Fangsheng OMV-FS380 vacuum deposition system under a pressure of  $< 5 \times 10^{-4}$  Pa. The organic films, LiF and aluminum were deposited according to

the OLED configurations at deposition rates of 1~2 Å s<sup>-1</sup>, 0.1 Å s<sup>-1</sup> and 3~5 Å s<sup>-1</sup>, respectively. The active area of each device was 3 mm × 3 mm.

The luminance–voltage–current density characteristics and EL spectra of monochromatic OLEDs were obtained by a Konica Minolta CS-200 Color and Luminance Meter and an Ocean Optics USB 2000+ spectrometer, along with a Keithley 2400 Source Meter. The external quantum efficiencies were estimated utilizing the normalized EL spectra and the current efficiencies of the devices. For hybrid two-color white OLEDs, the luminance–voltage–current density characteristics, electroluminescence spectra and external quantum efficiencies were obtained via a PhotoResearch PR670 spectroradiometer, with a Keithley 2400 Source Meter. All measurements were done at room temperature under ambient conditions for these devices.

EML	$\lambda_{\text{EL}}^{[a]}$ [nm]	$V_{\text{on}}^{[b]}$ [V]	$L^{[c]}$ [cd m <sup>-2</sup> ]	$\eta_{\text{c}}^{[c]}$ [cd A <sup>-1</sup> ]	$\eta_{\text{p}}^{[c]}$ [lm W <sup>-1</sup> ]	$\eta_{\text{ext}}^{[c]}$ max/ at 1000 cd/m <sup>2</sup> [%]	CIE (x, y) <sup>[d]</sup>
ITO/HATCN (5 nm)/TAPC (50 nm)/TCTA (5 nm)/EML (20 nm)/TPBi (40 nm)/LiF (1 nm)/Al (120 nm)							
CBP: 10% PT-1	412	3.2	3530	2.42	2.38	6.25/5.27	(0.153, 0.065)
CBP: 20% PT-1	414	3.2	5030	3.02	2.97	6.72/5.61	(0.151, 0.072)
mCP: 10% PT-1	408	3.4	3082	1.89	1.63	5.14/4.61	(0.153, 0.065)
mCP: 20% PT-1	414	3.2	4944	2.81	2.65	5.99/4.88	(0.152, 0.076)
CzSi: 10% PT-1	404	3.8	1841	1.90	1.42	6.24/3.30	(0.154, 0.062)
CzSi: 20% PT-1	408	3.6	3032	2.74	2.16	6.35/4.60	(0.152, 0.075)
CBP: 10% PT-2	408	3.2	3243	2.21	2.04	5.24/4.24	(0.152, 0.069)
CBP: 20% PT-2	414	3.2	4731	2.86	2.69	5.32/4.56	(0.151, 0.082)
mCP: 10% PT-2	408	3.4	2934	1.83	1.51	4.56/3.77	(0.153, 0.067)
mCP: 20% PT-2	414	3.4	4693	2.62	2.22	5.44/4.71	(0.152, 0.080)
CzSi: 10% PT-2	404	3.8	1992	1.75	1.25	5.04/3.12	(0.153, 0.066)
CzSi: 20% PT-2	414	3.6	3603	2.82	2.25	5.34/4.16	(0.151, 0.085)

**Table S4.** EL performances of the doped OLEDs based on PT-1 and PT-2 by tuning the host materials and varying doping concentration.

<sup>[a]</sup> $\lambda_{\text{EL}}$  = EL maximum. <sup>[b]</sup> $V_{\text{on}}$  = turn-on voltage at 1 cd m<sup>-2</sup>. <sup>[c]</sup>The luminescence ( $L$ ), current efficiency ( $\eta_c$ ), power efficiency ( $\eta_p$ ), external quantum efficiency ( $\eta_{\text{ext}}$ ). <sup>[d]</sup>CIE = Commission Internationale de L'Eclairage, recorded at 10 mA cm<sup>-2</sup>.

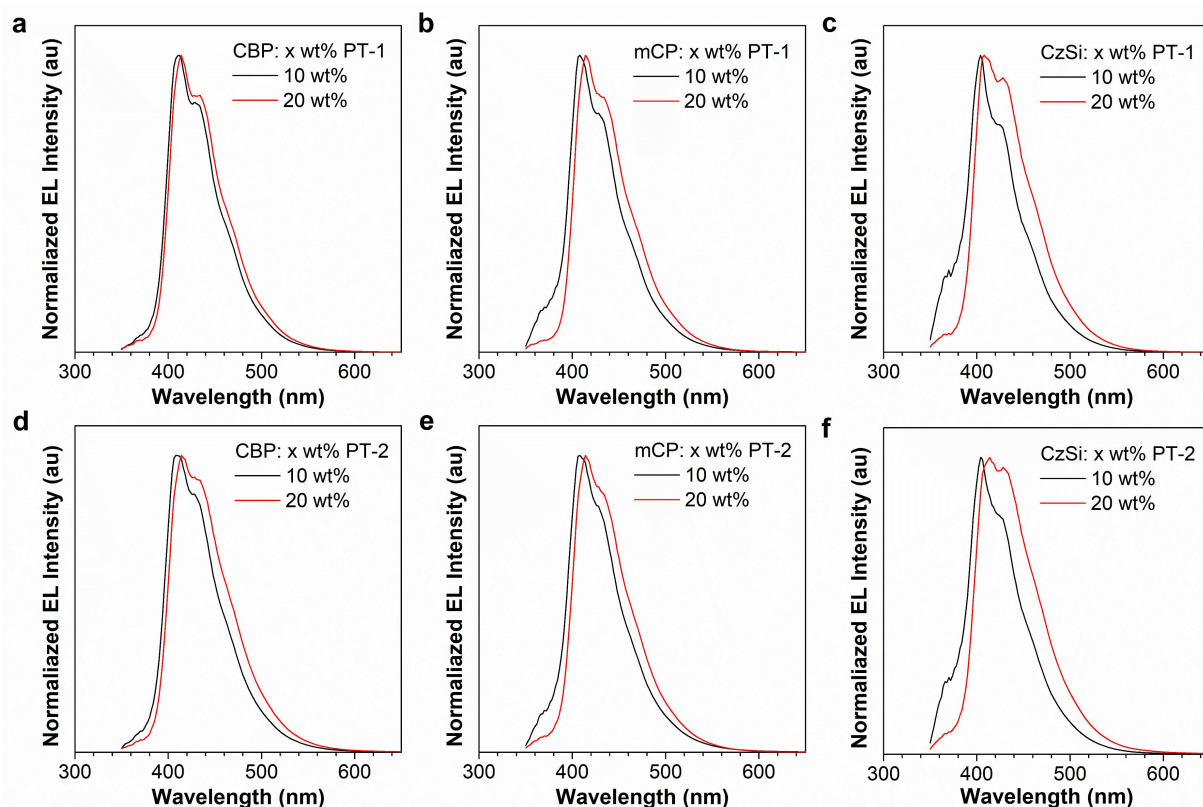


**Figure S8.** EL spectra of the doped OLEDs based on PT-1 and PT-2 by tuning the host materials and varying doping concentration.

### Design concept of the high-lying triplet states for “hot exciton” material

In order to realize the utilization of triplet excitons, the high-lying triplet states play a key role in "hot exciton" mechanism. For realization of this mechanism, the key of material design is how to suppress the internal conversion (IC) process of  $T_n \rightarrow T_1$  and construct effectively hRISC channels from triplet excitons at high-lying states ( $T_n \geq 2$ ) to singlet excitons.<sup>[6]</sup> Firstly, building blocks with a large  $T_2 - T_1$  gap to suppress the IC process, such as naphthalene, phenanthrene and anthracene, were generally chosen. And their derivatives often inherited this characteristic, by reviewing related literatures.<sup>[7]</sup> In addition, the introduction of appropriate heteroatoms may effectively promote the electron spin flip by using the El-sayed rule,<sup>[8]</sup> so as to capture more triplet excitons. Furthermore, the design concept of cross long-short axis is adopted to realize the introduction of CT components at high-lying level.<sup>[9]</sup>

For example,  $S_1$  and  $T_1$  have the same electronic configuration and show the characteristics of LE state or HLCT state, while high-lying triplet states ( $T_n \geq 2$ ) have stronger CT characteristics, which makes the binding energy of high-lying triplet excitons weak. Meanwhile, the difference between the electronic configuration of  $T_n$  adjacent to  $S_1$  will increase their SOC,<sup>[10]</sup> so as to promote the hRISC process.

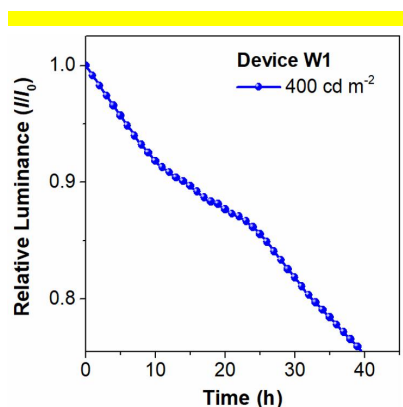


**Figure S9.** Relative luminance–time curves of device W1 at initial luminance of 400 cd m<sup>-2</sup>.

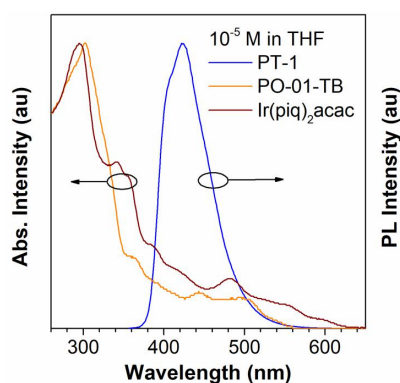


**Figure S10.** the PL spectrum of the host (PT-1) and the absorption spectrum of the guest (PO-01-TB and Ir(piq)<sub>2</sub>acac).

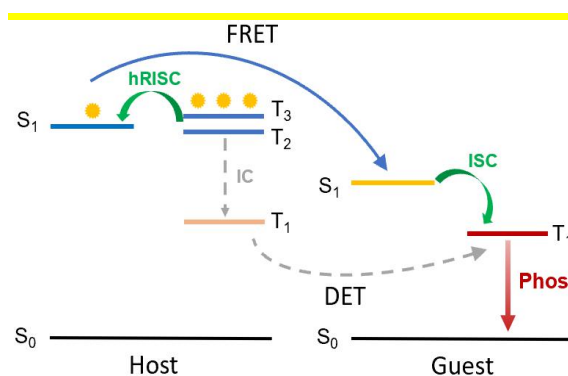


**Figure S11.** (a) Schematic diagram of energy transfer mechanism. S: singlet state; T: triplet

state; Phos.: phosphorescent; IC: internal conversion; hRISC: reverse intersystem crossing from high-lying triplet state. FRET: Förster resonance energy transfer; DET: Dexter energy transfer.

## 5. Reference

- [1] T. Lu, F. Chen, *J. Comput. Chem.* **2012**, *33*, 580.
- [2] B. A. Hess, C. M. Marian, U. Wahlgren, O. A. Gropen, *Chem. Phys. Lett.* **1996**, *251*, 365.
- [3] a) F. Neese, *J. Comp. Chem.* **2003**, *24*, 1740–1747; b) F. Neese, F. Wennmohs, A. Hansen, U. Becker, *Chem. Phys.* **2009**, *356*, 98–109.
- [4] S. Zhang, L. Yao, Q. Peng, W. Li, Y. Pan, R. Xiao, Y. Gao, C. Gu, Z. Wang, P. Lu, F. Li, S. Su, B. Yang, Y. Ma, *Adv. Funct. Mater.* **2015**, *25*, 1755–1762.
- [5] Z. R. Grabowski, K. Rotkiewicz, W. Rettig, *Chem. Rev.* **2003**, *103*, 3899–4031.
- [6] a) Y. Xu, P. Xu, D. Hu, Y. Ma, *Chem. Soc. Rev.* **2021**, *50*, 1030; b) X. Tang, R. Pan, X. Zhao, W. Jia, Y. Wang, C. Ma, L. Tu, Z. Xiong, *Adv. Funct. Mater.* **2020**, *30*, 2005765; c) Y. Xu, X. Liang, X. Zhou, P. Yuan, J. Zhou, C. Wang, B. Li, D. Hu, X. Qiao, X. Jiang, *Adv. Mater.* **2019**, *31*, 1807388;
- [7] Y. Y. Pan, J. Huang, Z. M. Wang, D. W. Yu, B. Yang, Y. G. Ma, *RSC Adv.* **2017**, *7*, 26697.
- [8] Y. Xu, C. Wang, X. Zhou, J. Zhou, X. Guo, X. Liang, D. Hu, F. Li, D. Ma, Y. Ma, *J. Phys. Chem. Lett.* **2019**, *10*, 6878
- [9] H. Zhang, A. Li, G. Li, B. Li, Z. Wang, S. Xu, W. Xu, B. Z. Tang, *Adv. Opt. Mater.* **2020**, *8*, 1902195.

[10] a) P. K. Samanta, D. Kim, V. Coropceanu, J. L. Bredas, *J. Am. Chem. Soc.* **2017**, *139*,

4042. b) H. Noda, X. K. Chen, H. Nakanotani, T. Hosokai, M. Miyajima, N. Notsuka, Y.

Kashima, J. L. Bredas, C. Adachi, *Nat. Mater.* **2019**, *18*, 1084;